


Distinct field-induced ferroquadrupolar states for two different magnetic-field directions in DyNiAl

Isao Ishii,* Daichi Suzuki, Tomohiro Umeno, Yuki Kurata, Yuki Wada, and Takashi Suzuki†
Department of Quantum Matter, AdSE, Hiroshima University, Higashi-Hiroshima 739-8530, Japan

Alexander V. Andreev

FZU Institute of Physics, Czech Academy of Sciences, Na Slovance 2, 182 21 Prague, Czech Republic

Denis I. Gorbunov, Atsuhiko Miyata, Sergei Zherlitsyn, and J. Wosnitza
*Hochfeld-Magnetlabor Dresden (HLD-EMFL) and Würzburg-Dresden Cluster of Excellence ct.qmat,
 Helmholtz-Zentrum Dresden-Rossendorf, 01328 Dresden, Germany*

 (Received 9 February 2021; revised 13 April 2021; accepted 13 May 2021; published 24 May 2021)

The hexagonal Dy-based compound DyNiAl undergoes ferromagnetic and antiferromagnetic-type magnetic phase transitions at $T_C = 30$ K and $T_1 = 15$ K, respectively. To investigate the $4f$ -electronic state and quadrupole interactions in DyNiAl, we carried out ultrasonic measurements versus temperature and applied magnetic field. The transverse elastic moduli C_{44} and C_{66} show a prominent elastic softening originating from an interlevel ferroquadrupolar-type interaction between the ground state and excited Kramers doublets, clarified by a crystal field analysis. In magnetic fields applied along the [100] and [001] axes, we observed a field-induced phase transition. Because the quadrupole interaction is enhanced in high magnetic fields according to our calculations, we suggest a magnetic-field-induced ferroquadrupolar ordering of the electric quadrupoles O_{xy} and O_{yz} for fields applied along [100] and [001], respectively, with different quadrupolar order parameters depending on the field direction.

DOI: [10.1103/PhysRevB.103.195151](https://doi.org/10.1103/PhysRevB.103.195151)

I. INTRODUCTION

Fascinating physical properties originating from the spin and orbital degrees of freedom, such as multipolar ordering and the (multichannel) Kondo effect, have attracted much attention. Such behavior appears especially in rare-earth-based compounds with localized f electrons [1–6]. The electric quadrupoles arising from the orbital degrees of freedom often play a central role for the underlying physical properties in these materials. We recently reported a ferroquadrupolar ordering and a magnetic-field-induced quadrupolar ordering in the Dy-based compounds DyNi₃Ga₉ and Dy₃Ru₄Al₁₂, respectively [7–10]. Under a trigonal (DyNi₃Ga₉) and hexagonal (Dy₃Ru₄Al₁₂) crystal electric field (CEF), the 16-fold multiplet of the Dy³⁺ ion with total angular momentum $J = 15/2$ splits into eight Kramers doublets with no quadrupole degeneracy. Because the energy splitting between the ground state and excited doublets is small in both compounds, the quadrupolar ordering occurs due to an interlevel quadrupole interaction between the ground and excited states. In other Dy-based compounds such as DyB₂C₂ and DyVO₄, a quadrupolar ordering was also reported [11,12].

In this paper, we investigate the Dy-based metallic compound DyNiAl with a hexagonal ZrNiAl-type structure (space

group: $P\bar{6}2m$) [13–19]. The Dy ions form a kagomelike triangular lattice in the (001) plane in this material. Dy-Ni and Al-Ni layers are stacked alternately along [001] [13]. The specific heat displays two peaks at $T_C = 30$ K and $T_1 = 15$ K, indicating successive phase transitions [16,18]. The magnetization $M(T)$ increases below T_C when a constant magnetic field of 0.1 T is applied along [001], suggesting a spontaneous magnetic moment. By contrast, $M(T)$ for a field applied along [120] decreases below T_C and changes the slope downward at T_1 [15,16]. The $M(H)$ for a field applied along [001] approaches the value of the full Dy moment, $10\mu_B$, below T_C already above 0.5 T [15,18]. The phase transition at T_C was proposed as a ferromagnetic (FM) ordering of the Dy magnetic moments aligned along [001]. Below T_1 , the Dy magnetic moments are tilted toward [100] from [001] with an antiferromagnetic (AFM) component in the (001) plane reported by neutron-diffraction experiments. [17] In addition, $M(H)$ for a field applied along [100] ([120]) at 4.2 K shows two anomalies around 1.8 and 12 (20) T [15,18].

The magnetic susceptibility χ follows a Curie-Weiss law above 140 and 30 K for [001] and [120], respectively [15]. The effective magnetic moments, $10.65\mu_B$, correspond to the theoretical value of the free Dy³⁺ ion, $10.63\mu_B$.

Ultrasonic measurements are an effective tool to investigate quadrupole interactions because, frequently, strain induced by ultrasound bilinearly couples to a corresponding quadrupole moment [20–30]. In our previous ultrasonic measurements on DyNiAl, an elastic softening of the transverse modulus C_{44} was observed as a characteristic behavior owing

*ish@hiroshima-u.ac.jp

†Also at Cryogenics and Instrumental Analysis Division, N-BARD, Hiroshima University, Higashi-Hiroshima 739-8530, Japan; tsuzuki@hiroshima-u.ac.jp

to the quadrupole interaction in the CEF [31]. To investigate the $4f$ -electronic state and quadrupole interaction in DyNiAl in detail, here we studied additional longitudinal and transverse elastic moduli using the ultrasonic technique at zero magnetic field and in applied fields, and analyzed the results within the CEF approach.

II. EXPERIMENTAL DETAILS

A DyNiAl single crystal was grown by a modified Czochralski method [15]. The lattice constants were determined to be $a = 6.998 \text{ \AA}$ and $c = 3.847 \text{ \AA}$ by x-ray powder diffraction experiments at room temperature. The sample was shaped in a rectangular parallelepiped of $1.80 \times 1.88 \times 2.67 \text{ mm}^3$. Temperature and field dependences of the elastic moduli C_{11} , C_{33} , C_{44} , and C_{66} were measured between 2 and 300 K and up to 17 T using a phase comparison-type pulse-echo method and orthogonal phase detection technique [32,33]. The propagation, \mathbf{k} , and displacement, \mathbf{u} , directions of the ultrasound are $\mathbf{k}||\mathbf{u}||[100]$ and $\mathbf{k}||\mathbf{u}||[001]$ for the longitudinal moduli C_{11} and C_{33} , respectively. C_{44} and C_{66} are transverse elastic moduli with $(\mathbf{k}||[001], \mathbf{u}||[100])$ and $(\mathbf{k}||[100], \mathbf{u}||[120])$, respectively. The modulus C was calculated using the relation $C = \rho v^2$, where $\rho = 7.578 \text{ g/cm}^3$ is the room-temperature mass density and v is the sound velocity. The absolute value of v was determined at 150 K using the sample length and a time interval between pulse echoes. We used LiNbO₃ transducers (ϕ 2 mm) with a fundamental resonance frequency of about 30 MHz for all modes and a pair of transducers were glued on the sample surfaces with room-temperature vulcanizing silicone or cyanoacrylate. The specific heat was measured using the relaxation method from 5 to 30 K and up to 9 T in a commercial physical property measurement system (PPMS). A magnetic property measurement system (MPMS) was used for magnetic-susceptibility measurements. The magnetic field was applied using a superconducting magnet in all measurements.

III. RESULTS AND DISCUSSION

A. Elastic modulus

Figure 1 shows the temperature dependences of the longitudinal elastic moduli C_{11} and C_{33} in DyNiAl. Both moduli increase monotonically with decreasing temperature down to 80 K. Below 80 K, an elastic softening of C_{11} is detected down to T_C . C_{11} exhibits an abrupt hardening at T_C and a steplike softening at T_1 . C_{33} also displays a slight softening below 80 K, and then shows an abrupt hardening at T_C . With further decreasing temperature, C_{33} continues to harden down to 2 K without any clear anomaly at T_1 . Obviously, the spin-lattice coupling does not produce a sizable anomaly for C_{33} at T_1 compared with the abrupt hardening below T_C .

Temperature dependences of the transverse elastic moduli C_{44} and C_{66} in DyNiAl are shown in Fig. 2. C_{44} exhibits a softening below 60 K, a change of the slope at T_C , and a hardening at T_1 . The elastic behavior of C_{44} below 150 K is consistent with previously reported results [31]. On the other hand, an elastic softening of C_{66} starts already around 130 K. C_{66} displays an abrupt hardening at T_C and a steplike softening at T_1 , similar to C_{11} .

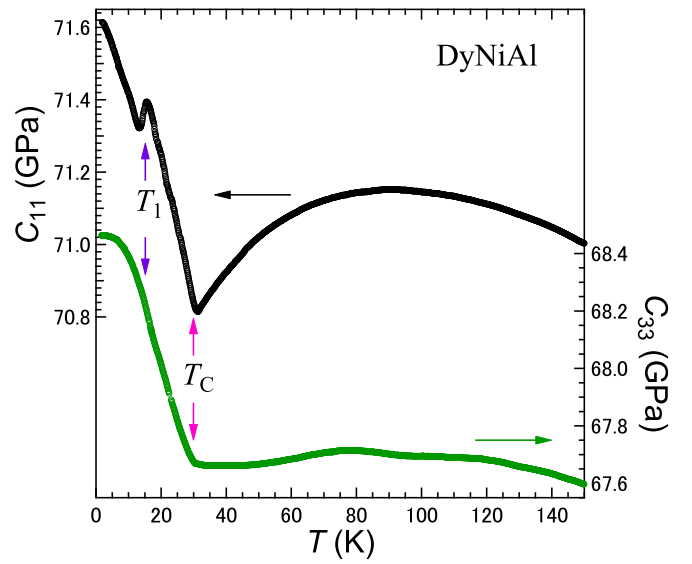


FIG. 1. Temperature dependences of the longitudinal elastic moduli C_{11} (left axis) and C_{33} (right axis) in DyNiAl. The vertical arrows indicate the phase transitions at T_C and T_1 .

B. Crystal-electric-field effects

The elastic softenings of the transverse moduli are a characteristic behavior arising from quadrupole interactions in a CEF. We performed a CEF analysis for C_{44} , C_{66} , $1/\chi$, and M in order to determine the $4f$ -electronic state and quadrupole interaction in DyNiAl. Here, we measured χ for a magnetic

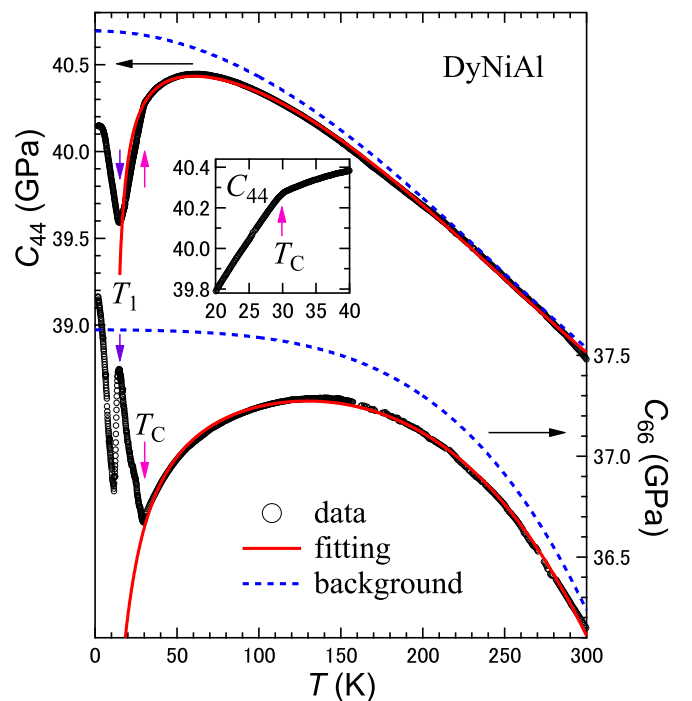


FIG. 2. Temperature dependences of the transverse elastic moduli C_{44} (left axis) and C_{66} (right axis) in DyNiAl. The vertical arrows indicate the phase transitions at T_C and T_1 . The inset shows C_{44} in the vicinity of T_C . The red solid and blue dashed lines show fit results and the background stiffness, respectively.

TABLE I. CEF parameters of DyNiAl in degrees Kelvin.

| B_2^0 | B_2^2 | B_4^0 | B_4^2 | B_4^4 | B_6^0 | B_6^2 | B_6^4 | B_6^6 |
|------------------------|------------------------|-----------------------|------------------------|-----------------------|-----------------------|-----------------------|------------------------|-----------------------|
| -4.96×10^{-1} | -9.50×10^{-3} | 1.33×10^{-4} | -2.00×10^{-5} | 3.20×10^{-5} | 1.91×10^{-6} | 7.00×10^{-6} | -1.15×10^{-5} | 5.86×10^{-4} |

field of 0.1 T applied along [100] and [001] between 2 and 300 K. The site symmetry of the Dy³⁺ ions in this structure is orthorhombic, C_{2v} [34]. Although there is a possibility that the local orthorhombicity is different between neighboring Dy ions strictly since the lattice symmetry is hexagonal, we adopted an orthorhombic CEF to simplify the analysis. We considered the following effective Hamiltonian H_{eff} :

$$H_{\text{eff}} = H_{\text{CEF}} + H_{\text{Q}} + H_{\text{ex}} + H_{\text{Zeeman}},$$

$$H_{\text{CEF}} = B_2^0 O_2^0 + B_2^2 O_2^2 + B_4^0 O_4^0 + B_4^2 O_4^2 + B_4^4 O_4^4 + B_6^0 O_6^0 + B_6^2 O_6^2 + B_6^4 O_6^4 + B_6^6 O_6^6,$$

$$H_{\text{Q}} = - \sum_i g_i O_i \varepsilon_i - \sum_i g'_i \langle O_i \rangle O_i \quad (i = 4, 6),$$

$$H_{\text{ex}} = - \sum_{j=A,B} J_{\text{ex}}^{AB} (\langle J_x \rangle^{(j)} J_x + \langle J_y \rangle^{(j)} J_y + \langle J_z \rangle^{(j)} J_z),$$

$$H_{\text{Zeeman}} = -g_J \mu_B J \cdot H,$$

where H_{CEF} , H_{Q} , H_{ex} , and H_{Zeeman} are Hamiltonians of the CEF, the quadrupole interaction, the spin-exchange interaction in the mean-field approximation, and the Zeeman interaction, respectively. Here, ε_i , g_i , g'_i , O_i , B_m^n ($n = 0, 2, 4, 6$ and $m = 2, 4, 6$), and O_m^n are the strain, the strain-quadrupole coupling constant, the quadrupole-quadrupole coupling constant, the quadrupole operator, the CEF parameter, and the Stevens equivalent operators, respectively [35]. $\langle O_i \rangle$, $\langle J_x \rangle$, $\langle J_y \rangle$, and $\langle J_z \rangle$ represent thermal averages. The subscripts $i = 4$ and 6 are equal to yz and xy . C_{44} and C_{66} are the linear responses to the ε_{yz} and ε_{xy} strains, which couple to the electric quadrupoles O_{yz} and O_{xy} , respectively. The subscripts x , y , and z correspond to [100], [120], and [001], respectively. The quadrupole interaction term H_{Q} is written only for C_{44} and C_{66} .

The temperature dependence of the elastic modulus C_{ii} is calculated using the following equation,

$$C_{ii}(T) = C_0 \left[\frac{1 - (N_0 g_i^2 / C_0 + g'_i) \chi_s(T)}{1 - g'_i \chi_s(T)} \right],$$

where N_0 ($=1.84 \times 10^{28} \text{ m}^{-3}$) is the number of Dy³⁺ ions per unit volume at room temperature and χ_s is the strain susceptibility [36,37]. We assumed the following temperature dependence of the background stiffness, $C_0 = a + bT^2 + cT^4$, where a , b , and c are constants determined by fits [38].

We adopted H_{ex} in the FM ordered state for the calculation of $1/\chi$ and M . To simplify the analysis, an intersublattice spin-exchange interaction J_{ex}^{AB} is included, whereas the intrasublattice interaction is excluded, where the symbols A and B refer to two sublattices [39]. $1/\chi$ and M were calculated using the above CEF model [40–42].

To reproduce C_{44} , C_{66} , and $1/\chi$, we carried out the CEF fits by using different initial values for the CEF parameters. Then, we changed all parameters in various combinations in order to reproduce the elastic moduli in an applied field and

M . The red solid curves in Fig. 2 are the best fits above T_C , i.e., in the nonordered state. The softenings of both C_{44} and C_{66} are well reproduced by our calculations with the fit parameters listed in Tables I and II. These parameters were determined to reproduce the elastic softenings of C_{44} and C_{66} at zero magnetic field and qualitatively in an applied field, as explained in detail in Sec. III D.

Within our analyses to reproduce all data, we established a CEF level scheme as shown in Fig. 3(a). The $4f$ -electronic state of the Dy³⁺ ion ($J = 15/2$) splits into eight Kramers Γ_5 doublets in the orthorhombic CEF. No elastic softening occurs when taking into account only the ground-state doublet, because the Kramers doublet possesses no quadrupole degeneracy. Our fit results reveal that the softening of the transverse moduli originates from the interlevel quadrupole interaction between the ground state and excited doublets. The positive sign of g' for both C_{44} and C_{66} (Table II) indicates that the interactions are of ferroquadrupolar type. In our preliminary work, we reported an antiferroquadrupolar-type interaction for C_{44} using a simplified analysis based on a Curie-Weiss-type formula [31]. We tried to describe C_{44} using a negative g' in the present work. However, C_{44} is better reproduced using a positive g' in our advanced analysis.

Below T_C , both moduli are not reproduced by the calculations, because the interlevel quadrupole interaction changes due to splitting of the CEF states by the FM ordering. The longitudinal modulus C_{11} also shows a softening below 80 K, as shown in Fig. 1. Since C_{11} is affected by the elastic behavior of $(C_{11} - C_{12})/2$, that is degenerate with C_{66} in the hexagonal symmetry, the softening of C_{11} is due to the quadrupole interaction corresponding to $(C_{11} - C_{12})/2$, such as in UCu₂Sn and DyNi₃Ga₉ [7,20].

The fit results for $1/\chi$ vs T and M vs H are shown in Figs. 3(b) and 3(c), respectively. $1/\chi$ for $\mathbf{H}||[100]$ and $\mathbf{H}||[001]$ including the data below T_C are well reproduced using $J_{\text{ex}}^{AB} = 1.20$ K, which is determined to reproduce T_C . The obtained ferromagnetic interaction J_{ex}^{AB} is consistent with the reported ferromagnetic structure [15,17]. For M with a magnetic field applied along [100] and [120], the phase transition around 1.8 T is well explained by the calculations. M for a field applied along [001] is also qualitatively reproduced except that the calculations produce a spontaneous magnetization of nearly the value of the full Dy³⁺ moment in low fields. On the other hand, the upturn around 12 and 20 T in the magnetization curves along [100] and [120], respectively,

TABLE II. Fitting parameters of the transverse moduli: $|g_i|$ (K), g'_i (K), a (GPa), b ($\times 10^{-6}$ GPa/K²), and c ($\times 10^{-11}$ GPa/K⁴).

| | $ g_i $ | g'_i | a | b | c |
|----------|---------|-----------------------|-------|--------|--------|
| C_{44} | 10.43 | 6.30×10^{-2} | 40.69 | -27.06 | 7.54 |
| C_{66} | 24.28 | 1.64×10^{-5} | 37.63 | -2.34 | -14.57 |

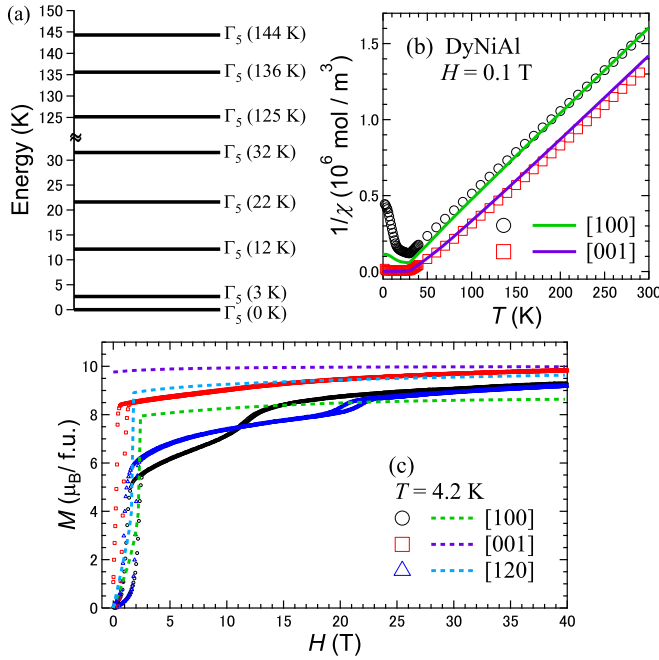


FIG. 3. (a) The $4f$ -level scheme for DyNiAl obtained from the CEF parameters listed in Table I, where Γ_5 denotes the irreducible representation for the point symmetry C_{2v} . (b) Temperature dependences of the inverse magnetic susceptibility measured in 0.1 T. (c) Magnetization curves at 4.2 K. The calculated results are shown by (b) solid and (c) dashed lines. The magnetization data were taken from Ref. [15].

cannot be explained within our CEF model. The upturn is caused by a phase transition, as discussed in Sec. III E. From these analyses, we were able to obtain the $4f$ CEF level scheme in DyNiAl.

C. Elastic modulus and specific heat in applied fields

To investigate the ordered states in DyNiAl in detail, we carried out ultrasonic and specific-heat measurements in applied magnetic fields. Figures 4(a) and 4(b) show the temperature dependences of C_{66} in fields applied along [100]. At low fields, elastic anomalies at both T_C and T_1 are observed. The steplike softening at T_1 becomes small with increasing field and is not detected above 1 T. The results obtained at 2 and 2.5 T show a peak structure below T_C . It is noteworthy that the temperature dependence in the vicinity of the phase transition changes drastically above 2.5 T, indicating that the type of the phase transition changes. C_{66} at $H \geq 3 \text{ T}$ shows a significant softening toward the phase transition which cannot be explained by spin-exchange interactions [7,20]. We label the characteristic temperature of this phase transition T_{Q1} . The softening enhances with increasing field and reaches the largest value of 6.7% at 7 T. At higher fields, the softening above T_{Q1} reduces gradually accompanied by a reduction of T_{Q1} . At $H \geq 12.8 \text{ T}$, another phase transition, labeled as T_{Q2} , is found around 6 K. The origin of the phase transitions at T_{Q1} and T_{Q2} , and the H - T phase diagrams of DyNiAl are discussed in Secs. III D and III E.

The field dependences of C_{66} for $H \parallel [100]$ up to 5 T at elevated temperatures are shown in Fig. 4(c). C_{66} exhibits an

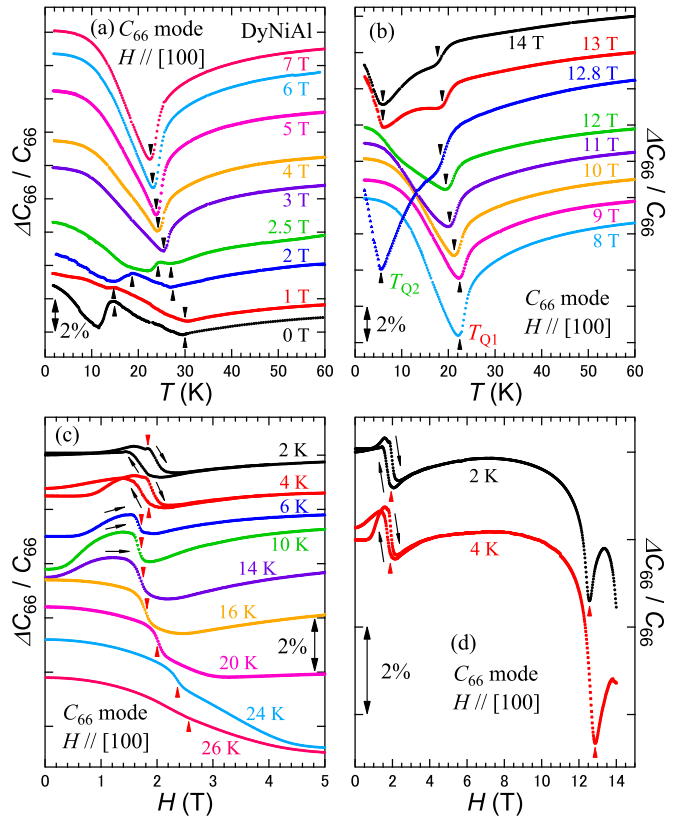


FIG. 4. (a), (b) Temperature and (c), (d) field dependences of the transverse elastic modulus C_{66} for $H \parallel [100]$. We plotted C_{66} as relative change $\Delta C/C$. The data are shifted for clarity. The vertical arrows indicate phase transitions.

abrupt softening at $H_1 \approx 1.8 \text{ T}$ accompanied by hysteresis. The magnetization curve for a field applied along [100] also shows hysteresis around this field [15], indicating that the field-induced transition at H_1 is of first order. Below 2 T, an elastic hardening is observed for $T \lesssim 15 \text{ K}$ and a softening for $T \gtrsim 15 \text{ K}$, reflecting a different ordered state below and above 15 K. Furthermore, in low magnetic fields, the critical field of the phase transition increases with temperatures above 15 K. Figure 4(d) shows data extended up to 14 T. C_{66} softens remarkably at 2 and 4 K above 8 T and exhibits a sharp minimum around 12.8 T which corresponds to the upturn in the field-dependent magnetization for $H \parallel [100]$ and T_{Q2} in the temperature dependences shown in Fig. 4(b) [15].

The temperature dependences of C_{44} for $H \parallel [100]$ are shown in Fig. 5(a). C_{44} displays anomalies at very similar temperatures as C_{66} . Akin to C_{66} , the behavior of C_{44} above 2.5 T changes drastically. For $H \geq 4 \text{ T}$, C_{44} also shows a softening toward T_{Q1} , however, the magnitude of the softening in C_{44} is smaller than for C_{66} and reduces rapidly with increasing field. In the field dependences, shown in Fig. 5(b), C_{44} exhibits a hardening around 1.8 T accompanied by hysteresis at $T \lesssim 15 \text{ K}$ and a kink around 2.3 T at $T \gtrsim 15 \text{ K}$. At high fields, a small minimum is observed around 12.8 T at 2 and 4 K, as shown in Fig. 5(c). The characteristic magnetic fields of the elastic anomalies in C_{44} correspond to those found for C_{66} .

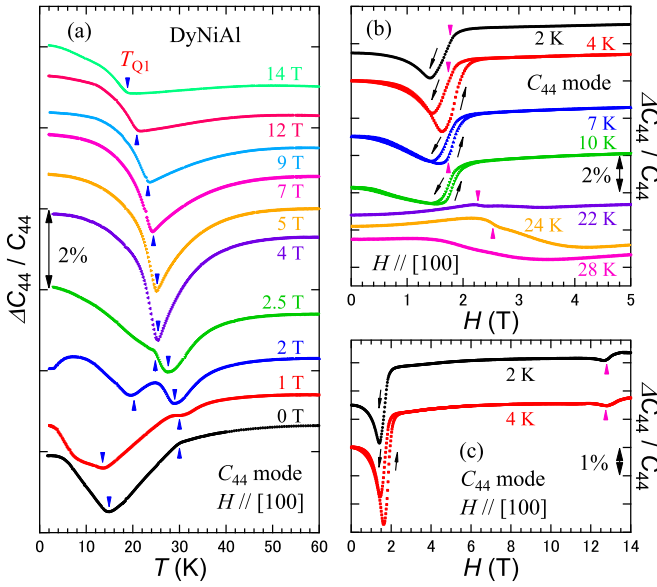


FIG. 5. (a) Temperature and (b), (c) field dependences of the transverse elastic modulus C_{44} for $H \parallel [100]$. The curves are vertically offset for clarity. The vertical arrows indicate phase transitions.

Figures 6(a) and 6(b) show the temperature dependences of C_{44} in fields applied now along [001]. Around 0.3 T, the change of the slope at T_C becomes unclear. By contrast, the minimum around T_1 remains, and the temperature of the minimum decreases gradually with increasing field. The magnitude of the softening below 60 K is hardly changed and the minimum survives up to 17 T. As shown in Figs. 6(c) and 6(d), C_{44} vs H at $T < 15$ K has an inflection point around 0.5 T, followed by softening up to 17 T.

The field dependences of C_{66} at $T < T_C$ exhibit an upturn around 0.5 T and the data at 9 K is accompanied by hysteresis below the magnetic field corresponding to H_1 [Fig. 6(e)]. This field is consistent with the field of the phase transition observed in the magnetization curve for a field applied along [001] [15]. The magnetization reaches almost the full moment of a free Dy^{3+} ion, $10\mu_B$, above 0.5 T, meaning that most of the Dy magnetic moments align along the field and are in the forced ferromagnetic state [Fig. 3(c)]. However, a minimum appears above 0.5 T in the temperature dependences of C_{44} , suggesting another phase transition of obviously not dipolar origin. We labeled the temperature of the minimum above 0.5 T in C_{44} as T_{Q3} .

To confirm the phase transition at T_{Q3} , we also measured the temperature dependences of C_{66} [Fig. 6(f)] and the specific heat C_p in magnetic fields applied along [001]. C_{66} exhibits, with decreasing temperature, a steplike softening at T_1 in zero field. This softening appears even above 0.5 T, and the position of this anomaly corresponds to T_{Q3} observed in C_{44} . T_{Q3} and the magnitude of the softening decrease with further increasing the field.

The temperature dependences of C_p in a magnetic field applied along [001] are shown in Fig. 7. A small peak is observed at T_1 in zero field [Fig. 7(a)]. The position of the small peak corresponds to the temperature of the elastic anomalies in C_{44} and C_{66} . The peak height and temperature decrease

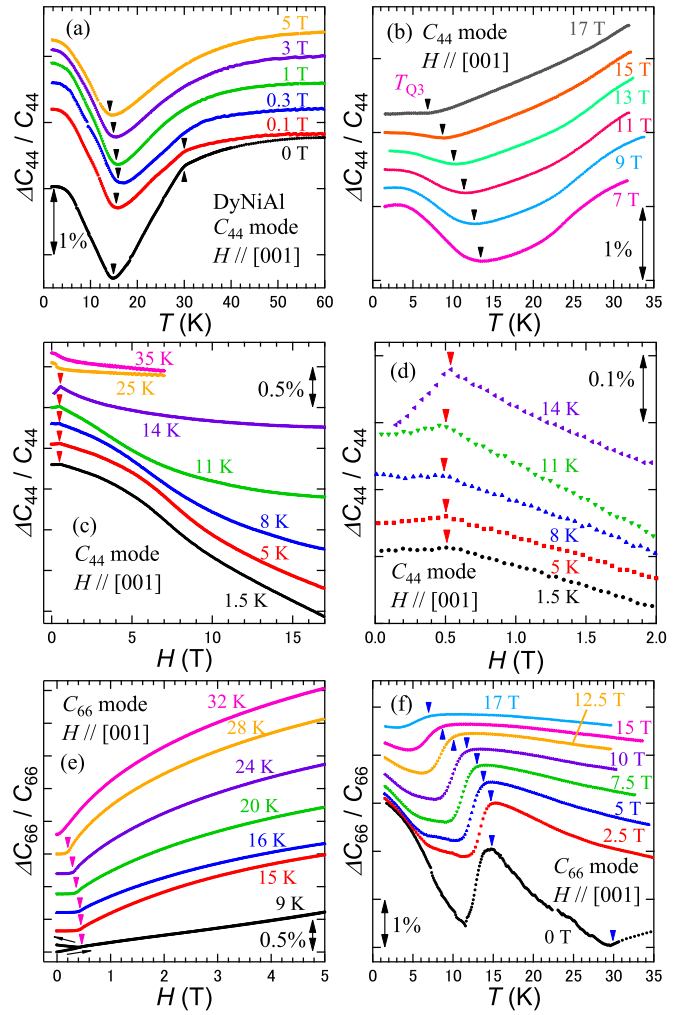


FIG. 6. (a), (b), (f) Temperature and (c), (d), (e) field dependences of the transverse elastic moduli C_{44} and C_{66} for $H \parallel [001]$. The curves are shifted along the y axis for clarity. (d) represents data at $T < 15$ K in an expanded scale below 2 T. The data at 9 K for C_{66} are shown for up and down sweeps. The vertical arrows indicate phase transitions.

gradually with increasing field and the peak is detected up to 9 T, confirming the phase transition at T_{Q3} .

In addition, C_p displays a sharp peak at T_C in zero field, as shown in Fig. 7(b). T_C decreases and the peak becomes broad at elevated magnetic fields. Above 0.6 T, no peak is detected at T_C . Generally, the FM transition temperature increases with increasing field, however, T_C decreases in DyNiAl. This may suggest that the FM ordering in DyNiAl is not a simple one.

We estimated the $4f$ -electronic contribution to the specific heat by subtracting the phonon contribution obtained on isostructural nonmagnetic LuNiAl from Ref. [43] and then evaluated the magnetic entropy at zero field. The released entropy at T_C reaches $15.4 \text{ J}/(\text{K mol})$ which exceeds $R \ln 6$, where R is the gas constant. This evidences that more than three doublets contribute to the specific heat up to T_C , which is in line with our CEF level analysis [Fig. 3(a)].

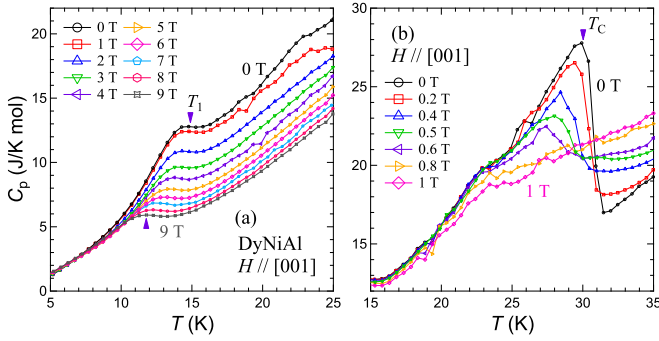


FIG. 7. Temperature dependences of the specific heat for $\mathbf{H}||[001]$ (a) from 5 to 25 K and (b) from 15 to 35 K.

D. Magnetic field-temperature phase diagram

From our results, we map out the H - T phase diagram of DyNiAl for $\mathbf{H}||[100]$ and $\mathbf{H}||[001]$ (Fig. 8). For $\mathbf{H}||[100]$, the phase boundary of the first-order transition at T_1 extends up to about 1.8 T [Fig. 8(a)]. T_C decreases with increasing field up to 2.5 T, and the field of the phase boundary decreases gradually with decreasing temperature. On the other hand, a magnetic-field-induced phase (FIP) at T_{Q1} emerges around 25 K and above 2.5 T. Another phase transition at T_{Q2} appears below 6 K and above 12.5 T and survives at least up to 14 T.

For $\mathbf{H}||[001]$, T_C decreases with increasing field [Fig. 8(b)]. Similar to the case of $\mathbf{H}||[100]$, the phase boundary has a maximum around 27 K at 0.8 T and then decreases down to 15 K and 0.5 T. The phase boundary to the AFM-type state extends up to about 0.5 T. Another phase transition appears at T_{Q3} around 15 K and above 0.5 T [Fig. 8(c)]. The corresponding FIP-III phase is followed at least up to 17 T.

Hereafter, we discuss the origin of the FIP transitions for both $\mathbf{H}||[100]$ and $\mathbf{H}||[001]$. The driving force of the FIP transitions cannot be explained by the exchange interactions,

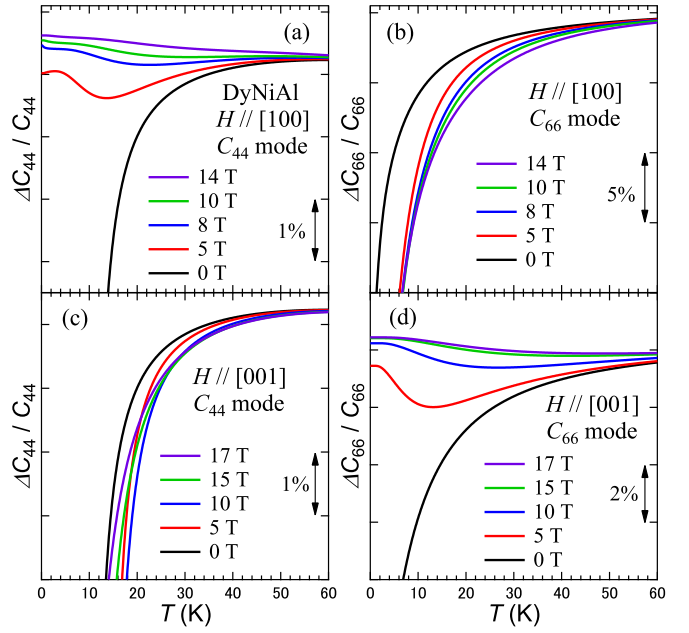


FIG. 9. Temperature dependences of the calculated (a) C_{44} and (b) C_{66} for $\mathbf{H}||[100]$, and (c) C_{44} and (d) C_{66} for $\mathbf{H}||[001]$.

as described above. We have revealed that the quadrupole interactions of O_{yz} and O_{xy} corresponding to the C_{44} and C_{66} modes, respectively, strongly affect the physical properties of DyNiAl. To assess the influence of the quadrupole interactions in magnetic fields, we calculated C_{44} and C_{66} in the nonordered state first using the parameters listed in Tables I and II. Figures 9(a) and 9(b) show the results for C_{44} and C_{66} , respectively, and $\mathbf{H}||[100]$. The elastic softening in C_{44} is suppressed by applying a field in contrast to C_{66} , of which the softening enhances with increasing field. For $\mathbf{H}||[001]$, the calculated results display completely different behavior, as

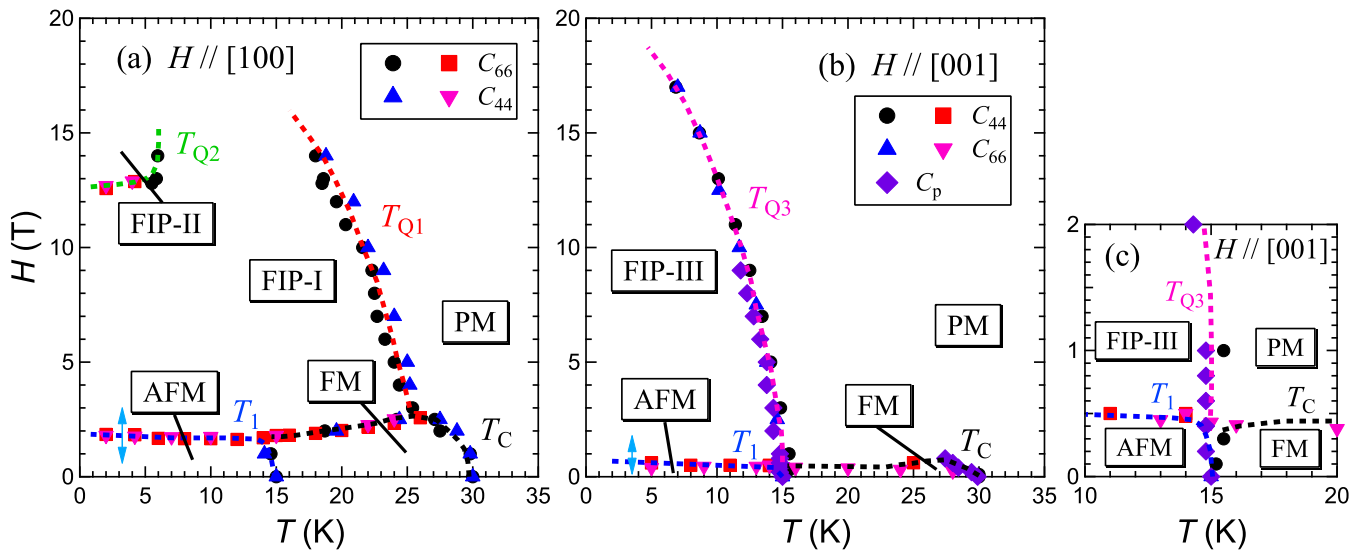


FIG. 8. H - T phase diagram for (a) $\mathbf{H}||[100]$ and (b) $\mathbf{H}||[001]$ of DyNiAl. The dashed lines are guides for the eye. Purple diamonds in (b) represent the phase boundary determined from the specific-heat measurements. Bidirectional blue arrows point out first-order phase transitions. PM and FIP stand for the paramagnetic state and magnetic-field-induced phase, respectively. (c) The same phase diagram for $\mathbf{H}||[001]$ in an expanded scale around 15 K and below 2 T.

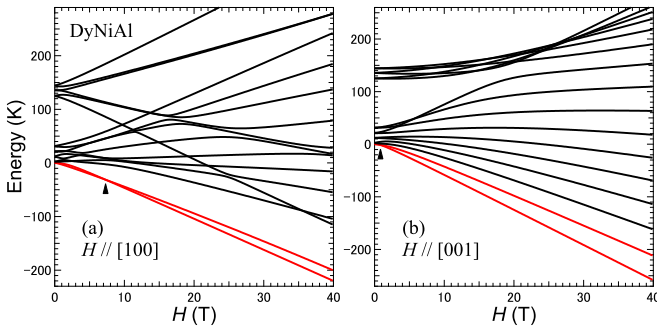


FIG. 10. Field dependences of the calculated CEF energies for (a) $\mathbf{H}||[100]$ and (b) $\mathbf{H}||[001]$. The two lowest states are depicted by red solid lines. The arrows indicate the field of the level crossing between the two lowest states.

shown in Figs. 9(c) and 9(d). The magnitude of the softening of C_{44} slightly increases and that of C_{66} rapidly decreases with increasing field. These calculated results are qualitatively consistent with our experimental data [see Figs. 4(a), 4(b), 5(a), 6(a), 6(b), and 6(f)].

The difference depending on the field direction can be understood by the field dependences of the CEF energies and the magnitude of the matrix elements of the quadrupoles O_{yz} and O_{xy} . The field dependences of the CEF energies for $\mathbf{H}||[100]$ and $\mathbf{H}||[001]$, calculated using $H_{\text{CEF}} + H_{\text{Zeeman}}$, are shown in Figs. 10(a) and 10(b), respectively. For $\mathbf{H}||[100]$, the ground state exhibits a level crossing around 7.5 T and the energy splitting by the Zeeman energy is small up to high fields, meaning that the ground state is quasidegenerate. For $\mathbf{H}||[100]$, the wave functions of the $4f$ -electronic states are mixed by the Zeeman energy, and the ground state has a quadrupole interaction involving O_{xy} , corresponding to C_{66} . The magnitude of the quadrupole interaction enhances with increasing field, therefore, the softening of the calculated C_{66} increases [Fig. 9(b)].

By contrast, the ground state exhibits a level crossing below 1 T for $\mathbf{H}||[001]$. The energy splitting of the lowest states becomes large with increasing field. For this field direction, the lowest states have a quadrupole interaction involving O_{yz} , corresponding to C_{44} . The magnitude of the quadrupole interaction slightly increases up to 10 T, and then decreases with further increasing field owing to the Zeeman splitting. In consequence, the softening of the calculated C_{44} slightly enhances up to 10 T and reduces above 10 T. In this way, we can qualitatively explain the difference in mode behavior in magnetic fields by our calculations, supporting our CEF analysis.

Our CEF calculations unveiled that the two lowest states possess a quadrupole interaction which enhances with increasing field for both field directions. Since C_{44} and C_{66} show large elastic softening even at zero field, the quadrupolar interactions are relatively strong. At low fields, however, the phase transitions at T_C and T_1 have a dipolar origin because the spin-exchange interactions are stronger than the quadrupolar interactions. The magnetic phase boundaries of T_C and T_1 lie below 2.5 and 0.6 T for $\mathbf{H}||[100]$ and $\mathbf{H}||[001]$, respectively. The magnetization for a field applied along [001] reaches $9\mu_B$ at 10 T, suggesting that most of the Dy magnetic moments

are in the forced ferromagnetic state, while the magnetization for a field applied along [100] is $7\mu_B$ at 10 T [Fig. 3(c)] [15]. Taking this into account, a plausible scenario is that the quadrupole interaction becomes dominant at the FIP transitions.

E. Driving force of the FIP transitions

When entering the FIP-I phase ($\mathbf{H}||[100]$), C_{66} shows a significant softening toward T_{Q1} which is most pronounced around 7 T [Figs. 4(a) and 4(b)], and the interaction involving O_{xy} enhances, suggesting it as the driving force of the phase transition. Here, the magnetization for a field applied along [100] jumps around 1.8 T and does not reach saturation below 12 T [15]. We consider two possible scenarios for the FIP-I phase. One is a magnetic-field-induced O_{xy} -type ferroquadrupolar ordering coexisting with spin order ($g' > 0$ for C_{66} , Table II). The other possibility would be a magnetic-field-induced octupolar ordering. This is because the two lowest states for $\mathbf{H}||[100]$ have large values of the matrix elements of magnetic octupoles T_y^α and T_y^β [2,44], although the coupling constant for these octupoles is unknown.

At T_{Q2} , the magnetization for a field applied along [100] displays an upturn and becomes almost saturated [15]. The field dependences of C_{66} at 2 and 4 K show a remarkable softening toward T_{Q2} [Fig. 4(d)]. By contrast, the small minimum at T_{Q2} observed in C_{44} [Fig. 5(c)] suggests that the ε_{xy} strain, corresponding to the quadrupole O_{xy} , is also related to the FIP-II phase. The phase transition at T_{Q2} might be caused by a modulation of the FIP-I ordered state, by changing that most of the magnetic components are aligned along [100].

For $\mathbf{H}||[001]$, the magnetization is almost saturated above 0.5 T. C_{44} shows a large softening toward T_{Q3} [Figs. 6(a) and 6(b)], and the quadrupolar interaction of O_{yz} enhances for this field direction. We propose that the phase transition at T_{Q3} (FIP-III) might be a magnetic-field-induced O_{yz} -type ferroquadrupolar ordering, because $g' > 0$ for C_{44} .

In the distorted kagome-lattice compound $\text{Dy}_3\text{Ru}_4\text{Al}_{12}$, we obtained the antiferroquadrupolar-type coupling constant from a CEF analysis. We proposed a magnetic-field-induced quadrupolar ordering and a geometrically frustrated alignment of the electric quadrupoles on each Dy^{3+} ion of the kagome lattice [10]. Since here ferroquadrupolar-type interactions are assumed in DyNiAl , the effect of geometrical frustration of the quadrupoles on the kagomelike triangular lattice may be weak.

For both H - T phase diagrams in DyNiAl , common features are that the FM and AFM-type phases are limited to the low-field range and magnetic-field-induced ferroquadrupolar (multipolar) ordering emerges at higher fields. The difference in the two phase diagrams for the two field orientations is the temperature range of the FIP states; T_{Q1} is higher than T_{Q3} for all magnetic fields applied in our experiments. This difference can be explained by the magnitude of the quadrupole interactions, including the magnitude of the matrix elements of the quadrupoles and the Zeeman splitting for the two lowest states. Since the interaction of O_{xy} for $\mathbf{H}||[100]$ is stronger than that of O_{yz} for $\mathbf{H}||[001]$, T_{Q1} is higher than T_{Q3} .

From another perspective, T_{Q1} and T_{Q3} appear just above the magnetic phase boundaries of T_C and T_1 , respectively

(Fig. 8). Elastic softening down to T_C is observed for C_{66} in contrast to C_{44} which softens down to T_1 (Fig. 2). The phase transitions at T_C and T_1 might suggest a ferroquadrupolar ordering of O_{xy} and O_{yz} at T_{Q1} and T_{Q3} , respectively. Although spin-exchange interactions are dominant at low fields, the quadrupole interactions start playing a central role at high fields, making DyNiAl a unique compound. Consequently, our results evidence magnetic-field-induced ferroquadrupolar ordering with a different order parameter of the electric quadrupoles depending on the field direction. In future works, because the CEF analysis was carried out by using the simple orthorhombic CEF model, neutron diffraction and resonant x-ray scattering experiments are required in order to clarify the ordered structure precisely.

IV. CONCLUSION

We performed ultrasonic measurements on DyNiAl down to 2 K and up to 17 T. At zero field, a prominent elastic softening was found in the transverse moduli C_{44} and C_{66} . A theoretical analysis using the orthorhombic CEF model was carried out for the transverse elastic moduli, magnetic susceptibilities, and magnetization data. We determined the $4f$ -electronic state in DyNiAl, revealing that the softenings of C_{44} and C_{66} are caused by the interlevel quadrupole interaction

between the CEF states. H - T phase diagrams for $\mathbf{H}||[100]$ and $\mathbf{H}||[001]$ were mapped out with magnetic-field-induced phase transitions emerging for both field directions. It follows from our calculations based on the CEF model that the most likely origin of the field-induced phases is ferroquadrupolar ordering of the electric quadrupoles O_{xy} and O_{yz} for $\mathbf{H}||[100]$ and $\mathbf{H}||[001]$, respectively.

ACKNOWLEDGMENTS

This work was supported by JSPS KAKENHI Grants No. 17H06136, No. 18KK0078, and No. 19K03719. This work was also supported by CResCent (Chirality Research Center) in Hiroshima University (the MEXT program for promoting the enhancement of research universities, Japan) and by JSPS Core-to-Core Program, A. Advanced Research Networks. The work was supported by Project No. 19-00925S of the Czech Science Foundation and by MGML [45] within the Program of Czech Research Infrastructures (Project No. LM2018096). We acknowledge the support of the High Magnetic Field Laboratory (HLD) at Helmholtz-Zentrum Dresden-Rossendorf (HZDR), a member of the European Magnetic Field Laboratory (EMFL), the Deutsche Forschungsgemeinschaft (DFG) through SFB 1143, and the Würzburg-Dresden Cluster of Excellence on Complexity and Topology in Quantum Matter – *ct.qmat* (EXC 2147, Project-id 390858490).

-
- [1] H. Sato, H. Sugawara, Y. Aoki, and H. Harima, in *Handbook of Magnetic Materials*, edited by K. H. J. Buschow (North-Holland, Amsterdam, 2009), Vol. 18, Chap. 1.
- [2] Y. Kuramoto, H. Kusunose, and A. Kiss, *J. Phys. Soc. Jpn.* **78**, 072001 (2009).
- [3] T. Onimaru and H. Kusunose, *J. Phys. Soc. Jpn.* **85**, 082002 (2016).
- [4] D. L. Cox, *Phys. Rev. Lett.* **59**, 1240 (1987).
- [5] Y. Yamane, T. Onimaru, K. Wakiya, K. T. Matsumoto, K. Umeo, and T. Takabatake, *Phys. Rev. Lett.* **121**, 077206 (2018).
- [6] T. Yanagisawa, H. Hidaka, H. Amitsuka, S. Zherlitsyn, J. Wosnitzer, Y. Yamane, and T. Onimaru, *Phys. Rev. Lett.* **123**, 067201 (2019).
- [7] I. Ishii, K. Takezawa, T. Mizuno, S. Kamikawa, H. Ninomiya, Y. Matsumoto, S. Ohara, K. Mitsumoto, and T. Suzuki, *J. Phys. Soc. Jpn.* **87**, 013602 (2018).
- [8] I. Ishii, K. Takezawa, T. Mizuno, S. Kumano, T. Suzuki, H. Ninomiya, K. Mitsumoto, K. Umeo, S. Nakamura, and S. Ohara, *Phys. Rev. B* **99**, 075156 (2019).
- [9] I. Ishii, K. Takezawa, H. Goto, S. Kamikawa, A. V. Andreev, D. I. Gorbunov, M. S. Henriques, and T. Suzuki, *J. Phys.: Conf. Ser.* **807**, 012002 (2017).
- [10] I. Ishii, T. Mizuno, K. Takezawa, S. Kumano, Y. Kawamoto, T. Suzuki, D. I. Gorbunov, M. S. Henriques, and A. V. Andreev, *Phys. Rev. B* **97**, 235130 (2018).
- [11] Y. Tanaka, T. Inami, S. W. Lovesey, K. S. Knight, F. Yakhou, D. Mannix, J. Kokubun, M. Kanazawa, K. Ishida, S. Nanao, T. Nakamura, H. Yamauchi, H. Onodera, K. Ohoyama, and Y. Yamaguchi, *Phys. Rev. B* **69**, 024417 (2004).
- [12] G. Gorodetsky, B. Lüthi, and B. M. Wanklyn, *Solid State Commun.* **9**, 2157 (1971).
- [13] G. Ehlers and H. Maletta, *Z. Phys. B* **101**, 317 (1996).
- [14] S. Daniš, P. Javorský, and D. Rafaja, *J. Alloys Compd.* **345**, 10 (2002).
- [15] A. V. Andreev, N. V. Mushnikov, T. Goto, and J. Prchal, *Physica B* **346–347**, 201 (2004).
- [16] J. Prchal, A. V. Andreev, P. Javorský, F. Honda, and K. Jurek, *J. Magn. Magn. Mater.* **272–276**, e419 (2004).
- [17] J. Prchal, P. Javorský, K. Prokeš, B. Ouladdiaf, and A. V. Andreev, *Physica B* **385–386**, 346 (2006).
- [18] J. Kaštil, P. Javorský, and A. V. Andreev, *J. Magn. Magn. Mater.* **321**, 2318 (2009).
- [19] N. K. Singh, K. G. Suresh, R. Nirmala, A. K. Nigam, and S. K. Malik, *J. Appl. Phys.* **99**, 08K904 (2006).
- [20] T. Suzuki, I. Ishii, N. Okuda, K. Katoh, T. Takabatake, T. Fujita, and A. Tamaki, *Phys. Rev. B* **62**, 49 (2000).
- [21] Y. Nemoto, T. Yamaguchi, T. Horino, M. Akatsu, T. Yanagisawa, T. Goto, O. Suzuki, A. Dönni, and T. Komatsubara, *Phys. Rev. B* **68**, 184109 (2003).
- [22] Y. Nakanishi, T. Sakon, M. Motokawa, M. Ozawa, T. Suzuki, and M. Yoshizawa, *Phys. Rev. B* **68**, 144427 (2003).
- [23] T. Yanagisawa, T. Goto, Y. Nemoto, S. Miyata, R. Watanuki, and K. Suzuki, *Phys. Rev. B* **67**, 115129 (2003).
- [24] T. Goto, Y. Nemoto, K. Sakai, T. Yamaguchi, M. Akatsu, T. Yanagisawa, H. Hazama, K. Onuki, H. Sugawara, and H. Sato, *Phys. Rev. B* **69**, 180511(R) (2004).
- [25] M. Akatsu, T. Goto, O. Suzuki, Y. Nemoto, S. Nakamura, S. Kunii, and G. Kido, *Phys. Rev. Lett.* **93**, 156409 (2004).

- [26] I. Ishii, H. Muneshige, Y. Suetomi, T. K. Fujita, T. Onimaru, K. T. Matsumoto, T. Takabatake, K. Araki, M. Akatsu, Y. Nemoto, T. Goto, and T. Suzuki, *J. Phys. Soc. Jpn.* **80**, 093601 (2011).
- [27] I. Ishii, H. Muneshige, S. Kamikawa, T. K. Fujita, T. Onimaru, N. Nagasawa, T. Takabatake, T. Suzuki, G. Ano, M. Akatsu, Y. Nemoto, and T. Goto, *Phys. Rev. B* **87**, 205106 (2013).
- [28] S. Kamikawa, I. Ishii, K. Takezawa, T. Mizuno, T. Sakami, F. Nakagawa, H. Tanida, M. Sera, T. Suzuki, K. Mitsumoto, and X. Xi, *Phys. Rev. B* **96**, 155131 (2017).
- [29] D. I. Gorbunov, T. Nomura, I. Ishii, M. S. Henriques, A. V. Andreev, M. Doerr, T. Stöter, T. Suzuki, S. Zherlitsyn, and J. Wosnitza, *Phys. Rev. B* **97**, 184412 (2018).
- [30] I. Ishii, T. Mizuno, S. Kumano, T. Umeno, D. Suzuki, Y. Kurata, T. Suzuki, D. I. Gorbunov, M. S. Henriques, and A. V. Andreev, *Phys. Rev. B* **101**, 165116 (2020).
- [31] D. Suzuki, I. Ishii, S. Kumano, T. Umeno, A. V. Andreev, D. I. Gorbunov, and T. Suzuki, *JPS Conf. Proc.* **30**, 011165 (2020).
- [32] T. J. Moran and B. Lüthi, *Phys. Rev.* **187**, 710 (1969).
- [33] B. Wolf, B. Lüthi, S. Schmidt, H. Schwenk, M. Sieling, S. Zherlitsyn, and I. Kouroudis, *Physica B* **294–295**, 612 (2001).
- [34] Ł. Gondek, J. Czub, A. Szytuła, Z. Izaola, and E. Kemner, *Solid State Commun.* **149**, 1596 (2009).
- [35] M. T. Hutchings, *Solid State Phys.* **16**, 227 (1964).
- [36] B. Lüthi, in *Dynamical Properties of Solids*, edited by G. K. Horton and A. A. Maradudin (North-Holland, Amsterdam, 1980), Chap. 4.
- [37] See Supplemental Material of Ref. [8].
- [38] M. Nohara, T. Suzuki, Y. Maeno, T. Fujita, I. Tanaka, and H. Kojima, *Phys. Rev. B* **52**, 570 (1995).
- [39] M. Sera, H. Nohara, M. Nakamura, H. Tanida, T. Nishioka, and M. Matsumura, *Phys. Rev. B* **88**, 100404(R) (2013).
- [40] N. V. Hieu, T. Takeuchi, H. Shishido, C. Tonohiro, T. Yamada, H. Nakashima, K. Sugiyama, R. Settai, T. D. Matsuda, Y. Haga, M. Hagiwara, K. Kindo, S. Araki, Y. Nozue, and Y. Ōnuki, *J. Phys. Soc. Jpn.* **76**, 064702 (2007).
- [41] S. Kamikawa, I. Ishii, Y. Noguchi, H. Goto, T. K. Fujita, F. Nakagawa, H. Tanida, M. Sera, and T. Suzuki, *J. Phys. Soc. Jpn.* **85**, 074604 (2016).
- [42] See Supplemental Material of Ref. [29].
- [43] P. Javorský, M. Diviš, H. Sugawara, H. Sato, and H. Mutka, *Phys. Rev. B* **65**, 014404 (2001).
- [44] R. Shiina, H. Shiba, and P. Thalmeier, *J. Phys. Soc. Jpn.* **66**, 1741 (1997).
- [45] <https://mgml.eu>.